Analysis of additively manufactured flexible wing model

Rossana Fernandes, Benyang Hu, Zhichao Wang, Zheng Zhang and Ali Y. Tamijani Department of Aerospace Engineering, Embry-Riddle Aeronautical University, Daytona Beach, Florida, USA

Abstract

Purpose – This paper aims to assess the feasibility of additively manufactured wind tunnel models. The additively manufactured model was used to validate a computational framework allowing the evaluation of the performance of five wing models.

Design/methodology/approach – An optimized fighter wing was additively manufactured and tested in a low-speed wind tunnel to obtain the aerodynamic coefficients and deflections at different speeds and angles of attack. The flexible wing model with optimized curvilinear spars and ribs was used to validate a finite element framework that was used to study the aeroelastic performance of five wing models. As a computationally efficient optimization method, homogenization-based topology optimization was used to generate four different lattice internal structures for the wing in this study. The efficiency of the spline-based optimization used for the spar-rib model and the lattice-based optimization used for the other four wings were compared.

Findings – The aerodynamic loads and displacements obtained experimentally and computationally were in good agreement, proving that additive manufacture can be used to create complex accurate models. The study also shows the efficiency of the homogenization-based topology optimization framework in generating designs with superior stiffness.

Originality/value — To the best of the authors' knowledge, this is the first time a wing model with curvilinear spars and ribs was additively manufactured as a single piece and tested in a wind tunnel. This research also demonstrates the efficiency of homogenization-based topology optimization in generating enhanced models of different complexity.

Keywords Additive manufacturing, Wind tunnel model, Aeroelasticity, Homogenization, Topology optimization

Paper type Research paper

1. Introduction

Typical wind tunnel models are fabricated from metal, wood, foam and fiberglass. Their manufacturing can be expensive, time-consuming and complex. Adding to the difficulty of building complex geometries is the fact that the models must conform to certain standards of surface finishing and tolerances. In addition, the actual model and the prototype should have the same geometry, mass, stiffness, strength and dynamics (Zhu, 2019), which is not often straightforward because scaling the geometry only does not guarantee the same stiffness, strength and aerodynamics. Both structural and aerodynamic scaling methods are needed.

Researchers have found additive manufacturing (AM) as a potential replacement for traditional fabrication methods of wind tunnel models. AM can reduce the cost and build time, and fabricate complex shapes. Most common AM methods, such as stereolithography (SLA), selective laser sintering (SLS) and fused deposition modeling (FDM), take about one day to fabricate a plastic wind-tunnel model, whereas traditional ceramic or metal machined models take weeks to months to be built (Barlow et al., 1999; Aghanajafi and Daneshmand, 2010). This facilitates possible corrections to the models by cutting

The current issue and full text archive of this journal is available on Emerald Insight at: https://www.emerald.com/insight/1355-2546.htm



their fabrication time and effort. In addition, internal structures and elaborated geometries can be more easily fabricated from a computer-aided design (CAD) model through AM, contributing to the fulfillment of the mass and stiffness similarities (Zhu, 2019). The aforementioned advantages of AM address some of the hindrances of traditional methods, creating possibilities for new design concepts.

AM models also have challenges due to the nature of the fabrication method and the material used. The mechanical properties of AM structures highly depend on printing process parameters (Fernandes et al., 2021; Tsushima et al., 2021). Plastic models cannot usually endure several test cycles due to fatigue (Aghanajafi and Daneshmand, 2010) and are not reliable at high speeds due to their low stiffness and strength (Zhu et al., 2019b). Several researchers have attempted to

Competing interest: The authors declare that they have no known competing financial interests or personal relationships that could have appeared to influence the work reported in this paper.

The authors would like to thank the staff of the wind tunnel facility at Micaplex for their guidance and support in this project. The authors are also thankful to Dr Ebenezer Gnanamanickam, Associate Professor of Aerospace Engineering, for his guidance on the wind tunnel test. This research was supported by the US Air Force Office of Scientific Research (AFOSR) under award number FA9550-17-1-0171 and National Science Foundation (NSF) under award number 1847133. The authors would like to thank AFOSR and NSF for their support.

Received 29 March 2023 Revised 21 July 2023 Accepted 4 September 2023

Volume 30 · Number 1 · 2024 · 73-84

improve the stiffness of AM wind tunnel models (Zhu et al., 2019b; Kroll et al., 2010; Zhu et al., 2019a; Zhu et al., 2019b).

Despite the aforementioned limitations, researchers have successfully taken advantage of AM to facilitate their studies for the different regimes up to the hypersonic speed (Zhu et al., 2019b; Rêgo et al., 2018). Different types of wind tunnel models, such as aircraft (Zhu et al., 2019b; Raza et al., 2021; Chung et al., 2020), unmanned aerial vehicles (UAVs) (Goh, 2017; Junk et al., 2017) and missiles (Aghanajafi and Daneshmand, 2010) models, have been built through AM techniques demonstrating their viability. In fact, the low stiffness or large flexibility might be desirable and more representative of real models (Zhu et al., 2019b). Several authors (Su and Cesnik, 2011; Tsushima et al., 2021; del Carre et al., 2019) have developed geometric nonlinear aeroelastic models of flexible wings because they experience large deformations. Tsushima et al. (2021) used FDM to manufacture a flexible solid rectangular wing. The results from the wind tunnel test show a good agreement between the printed model and the computational results using the unsteady vortex lattice method and MacNeal-Schwendler Corporation (MSC). Nastran. Also, the layer-by-layer nature of commonly used AM methods not only affects the material properties but also results in a stair-stepping effect for some geometries and low-quality surface finish, requiring some post-processing such as sanding and painting (Zhu, 2019). Aghanajafi and Daneshmand (2010) have compared two missile models built of steel through binder jetting and machining. The aerodynamic coefficients from the wind tunnel test showed that the difference between the two models becomes more tenuous with the increase of the Mach number. Due to the limited accuracy in the aerodynamic response obtained from the AM models, several authors (Kroll et al., 2010; Aghanajafi and Daneshmand, 2010) have advised using these models only at the early design stage.

Wind tunnel models are usually rigid, and deformation corrections are often applied to obtain a closer representation of the real models (Zhu et al., 2019b). One of the early attempts to additively manufacture a flexible wing model with internal structures was made by Pankonien et al. (2017). The model was tested in the wind tunnel at subsonic speeds (less than Mach 0.13). The different partitions of the wing were attached through interpenetrating fastening. This mechanism reduces the stress concentration and grants access to the interior. This interconnecting mechanism would be unfeasible for complex and more realistic models such as the one in the present study. The current research aims to use the flexibility of AM and build an elastic wing model with optimized internal structures.

The objectives of the present work are as follows:

- to create a robust computational framework to support an optimization framework in assessing the aeroelastic performance and efficiency of the optimized wing models;
- to develop a guideline for the wind tunnel test used to validate computational models;
- to demonstrate the practicality of AM in fabricating wind tunnel models for advanced concepts; and
- to demonstrate the feasibility of homogenization-based topology optimization in creating optimized designs that can be as simple as the curvilinear spar-rib model (by constraining the design parameters) or as detailed as lattice structures (by relaxing the design parameters).

2. Analysis of an additively manufactured flexible wing model

This section discusses the manufacturing and wind tunnel setup as well as the finite element analysis of the supersonic wing used in this study.

2.1 Wing model

A supersonic fighter wing was selected as the model in this study. The weight of the model that was optimized by Locatelli et al. (2011) was subjected to stress and buckling constraints. The particle-swarm optimization was performed considering the internal topology and size of the skin, spars and ribs as design variables. The optimized wing (2.40 m semi-span, 2.54 m root chord and 0.84 m tip chord) has curved spars and ribs, which have been shown to produce lighter designs with better aeroelastic and structural performance (Fernandes and Tamijani, 2017; Locatelli et al., 2011).

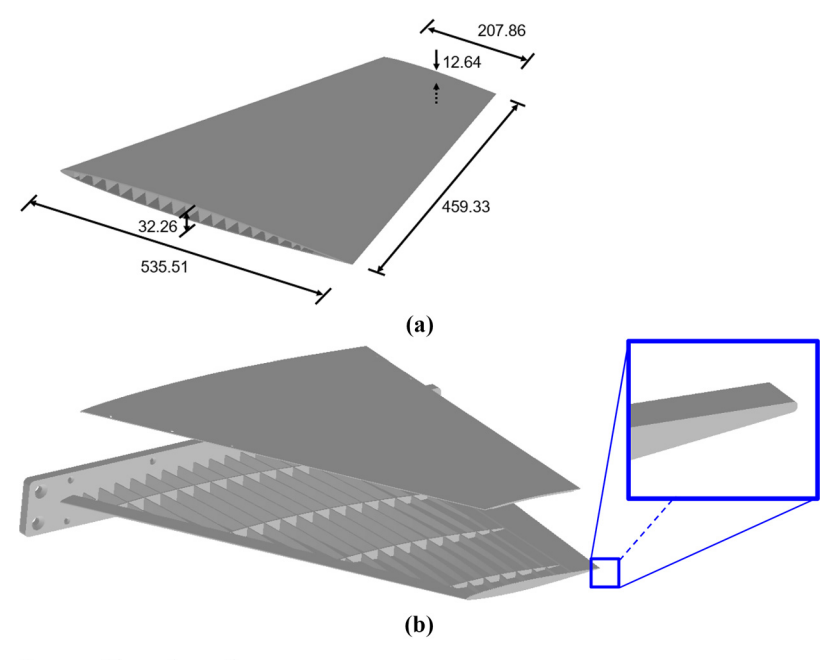
The planform model was geometrically scaled down by a factor of 5.20 due to the limitation of the manufacturing built volume. The dimensions of the wing shown in Figure 1 are different from the wing planform reported in the Locatelli *et al.*'s (2011) article. A 2.59 mm thickness was attributed to the skin, extending the chord by 11.03 mm at the leading edge and 35.44 mm at the trailing edge (TE) so that the top and bottom skin could meet in a single edge.

The model was further modified to comply with the manufacturing and test requirements discussed later. The geometry and size of the model are shown in Figure 1 and listed in Table 1. Initially, the model was printed in PA12 through SLS. However, due to its large dimensions and thin skin, as well as the nature of SLS (it operates at high temperatures and parts cool off at uneven rates), the residual stresses caused warping. Later, the wing was successfully printed without warping and with a smoother surface finish through SLA using a 3D Systems ProX 950 printer (Figure 2). The model was built layer-by-layer in the span direction. The build time was around 24 h for a layer thickness of $100 \, \mu m$. The material was chosen based on availability and properties. The selected Accura 25 is a resin similar to ABS and polypropylene. According to preliminary calculations, Accura 25 would resist the wind forces but would not be too stiff to prevent visible deformation. The material properties of Accura 25 were determined according to ASTM D638-14: $E=1377\,\mathrm{MPa}$, $\nu=0.37$ and $\rho=1190\,\mathrm{kg/m}^3$. As the data for the original airfoil NACA 65A004.8 was not available, the symmetric NACA 64A006 (Abbott and Von Doenhoff, 2012) was modeled instead. A blunt TE, shown in Figure 1(b), was considered because the sharp TE would be too thin to meet the minimum manufacturable thickness, which is discussed later in this article. However, this modification came with a compromise because blunt TEs cause flow recirculation and separation more upstream than the sharp counterpart (Thompson and Whitelaw, 1988).

The model was modified to account for the manufacturing and experimental constraints. The initial focus was satisfying the experimental requirements, which included adding a mounting base to the model to allow it to be properly attached to the wind tunnel turntable and force balance; not only scaling down the model below 457 mm span to allow detectable

Volume 30 · Number 1 · 2024 · 73-84

Figure 1 (a) Wing geometry with dimensions in mm (b) wing model showing bottom skin detached from the rest of the model and blunt trailing edge



Source: Figure by authors

Table 1 Summary of the model dimensions

Dimensions	Value
Semi-span (mm)	459.33
Root chord (mm)	535.51
Tip chord (mm)	207.86
Root airfoil thickness (mm)	32.26
Tip airfoil thickness (mm)	12.64
Quarter chord sweep angle (°)	24.03
Skin thickness (mm)	2.59
Spar thickness (mm)	1.73
Rib thickness (mm)	2.34
Source: Table by authors	

deformation with the apparatus used (not only because reducing the size increases the stiffness but also because the deformations would become difficult to capture through the glass window of the tunnel with the set of cameras outside); printing the model in more than one part was not desirable because printing only one part prevent surface irregularities and mismatches resulting from printing tolerances and gluing parts together; and applying modifications or using hardware should not disturb the wind flow.

With these four constraints in mind, the manufacturing constraints were also considered. They are as follows:

- For the AM technique, the maximum build volume was 1,500 × 750 × 550 mm, and the minimum feature size was 0.60 mm. Any feature smaller than that was changed to the minimum size.
- The bottom skin was printed separately, as shown in Figure 1(b), to allow any excess material to be removed after printing.

Escape holes through all the spars and ribs would not be as effective in eliminating the excess material and might compromise the structure's strength. The wing was, therefore, printed in two pieces. The cavity was created on the bottom of the wing, and its cover was glued (using a two-part epoxy) and sanded to remove any excess glue, ensure surface smoothness and reduce flow perturbation. SLA produced a smooth surface finish, not requiring further sanding elsewhere, to ensure a laminar boundary layer developing on the leading edge of the wing model. No boundary layer tripping was used on the wing.

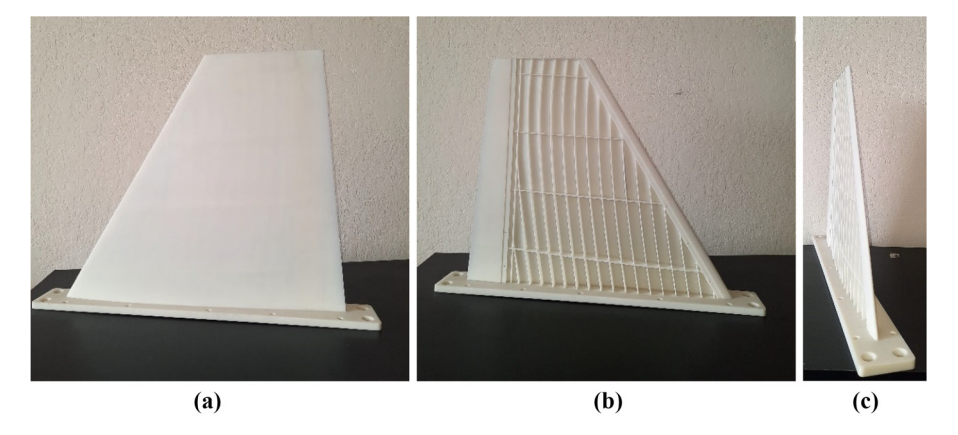
2.2 Wind tunnel and set-up

The semi-span wing model was tested in the MicaPlex low-speed wind tunnel facility at Embry-Riddle Aeronautical University. It is a closed circuit, closed test section wind tunnel. The rectangular cross-section of the test section [Figure 3(a) and (b)] is 1.80 m wide, 3.65 m long and 1.20 m tall. The maximum speed at the test section is 100 m/s (or Mach number 0.38). There are three layers of the turbulence screen in the settling chamber. The free-stream turbulence intensity measured is less than 0.10% at a lower tunnel speed of 50 m/s, as measured by a single-component hot-wire anemometry at 20 kHz. At the maximum speed, the turbulence intensity is slightly higher, i.e. 0.20%. The dynamic pressure at the test section is determined by the total pressure from a pair of pitot tubes mounted in the settling chamber and the static pressure ports at the inlet of the test section.

The wing was vertically mounted to the turntable on the floor of the test section, as shown in Figure 3(a) and (b). The plastic base of the wing model was attached to a thick aluminum plate for extra stiffness and then connected to the force balance with a steel post. The aluminum plate and the base of the wing were involved by a splitter plate and the fairing structure, which were built together and bolted to the turntable [Figure 3(c)].

Volume 30 · Number 1 · 2024 · 73-84

Figure 2 Additively manufactured wing model



Notes: (a) Top surface; (b) bottom surface without cover skin and showing internal

structures and (c) side view showing no warping

Source: Figure by authors

The splitter plate eliminates the boundary layer growth on the wind tunnel floor. The splitter plate was modeled according to the guidelines established by Diebold *et al.* (2015). The splitter plate and fairings were combined in a single part, eliminating the need for fasteners. The combined part was fabricated with SLS PA12 instead of the traditionally machined metal alloy plate, demonstrating the practicality of AM. The distance between the leading edge of the splitter plate and the wing leading edge is 25% of the chord at the root. The white splitter plate shown in Figure 3(c) is 273 mm wide and 6.35 mm thick, and its edge profile is based on the NACA 0012 airfoil.

2.3 Force measurement

An external pyramidal force balance was used to measure the aerodynamic loads and pitching moment on the wing. The force balance is located underneath the test section on a separate concrete foundation to reduce the noise due to the wind tunnel motor running. The balance system can measure six-component forces and moments, i.e. the axial, side and normal forces, as well as the roll, pitch and yaw moments. Because the semi-span wing model was mounted vertically in the test section, the lift was measured by the side-force component and the pitching moment was measured by the yaw component. The wing model was pivoted at the point that locates the quarter chord at the root.

The side-force component capacity is $\pm 2,224$ N, with a full-scale accuracy of 0.14% as quoted by calibration. The drag-force component measures the force up to 1,112 N with an accuracy of 0.20%. At each angle, the aerodynamic loads were sampled at 1,000 Hz for 15 s through an analog voltage input module to the data acquisition system. After removing the gravity tare, the average of the 15,000 samples is shown in the following sections.

2.4 Deformation measurement

The out-of-plane deflection of the wing model was measured with a high-speed digital image correlation (DIC) system. The system consists of two 4-megapixel complementary metal oxide semiconductor (CMOS) cameras with Nikon 60 mm micro-lenses.

Each camera has a resolution of $2,560 \times 1,600$ pixels at a frame rate of 1,400 Hz. The cameras collected 10 s of images at a sampling frequency of 100 Hz for a set speed and angle of attack (AOA). Two high-speed cameras were positioned outside the test section at approximately 90° from each other to form a stereoscopic set-up, as shown in Figure 3(a).

The model was painted black with a white random speckle pattern, shown in Figure 3(b). When the wing model was set to the angle of attack, and the wind was off, the reference images were taken. Then, the tunnel was set to the speed to acquire the aerodynamically induced deflection. The images were processed in the Correlated Solutions' commercial software VIC-3D with a subset size of 49 pixels.

2.5 Finite element model

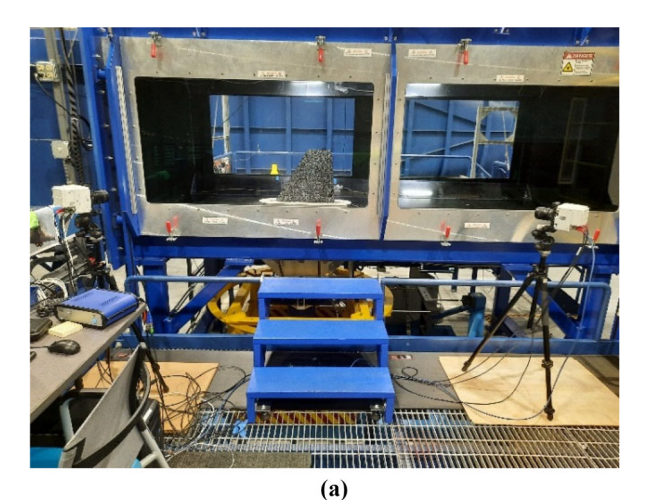
Three different groups were identified from the CAD model: the skin, spars and ribs. A brief inspection has shown that considering the base of the wing would not affect the results. Therefore, the base was ignored to reduce the mesh and computational time. The solid model was imported and meshed in Ansys using 1.3 million Tetra10 elements. The mesh convergence is discussed in Section 3.

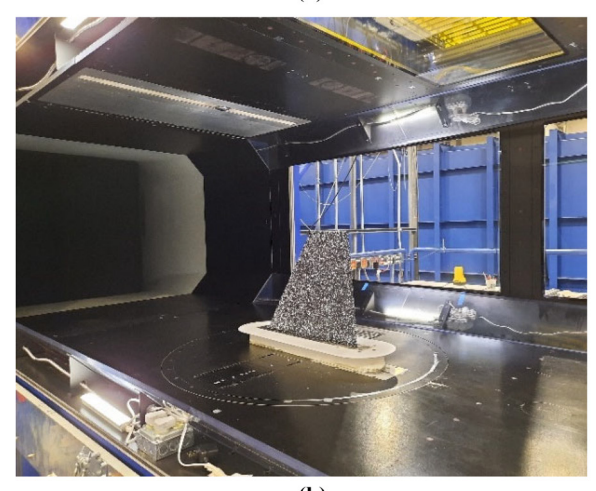
All degrees of freedom, except the out-of-plane translation (y-axis) and the rotation about the y-axis for the nodes at the wing root, were constrained. A torsional spring element about the y-axis was applied to those nodes. The springs had a stiffness close to the estimated torsional stiffness of the wing (70 kN m²). The translation in the y-axis for the nodes at the wing root midsurface was also constrained. These constraints were developed based on the observation of the experimental model.

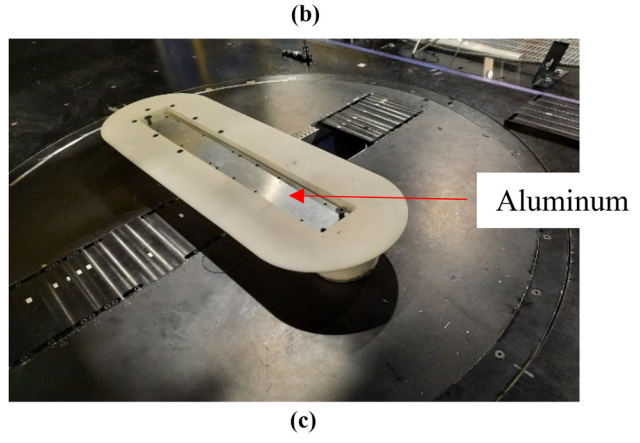
A MATLAB framework was developed to generate and run the Nastran input file (.bdf) for static structural and static aeroelasticity. The framework requires the user to provide the mesh, loading, boundary conditions, material properties and flow characteristics (Mach number, airspeed, air density, reduced frequency, dynamic pressure and angle of attack) for the case of aeroelastic analyses. In the aeroelastic analysis, the air density was $1.226 \, \text{kg/m}^3$; the loads were computed in a new $50 \times 50 \, \text{grid}$ (aerodynamic boxes), shown in Figure 4, and the displacements were computed in the structural grid. The

Volume 30 · Number 1 · 2024 · 73–84

Figure 3 The AM wing model, splitter plate and fairing-mounted in the wind tunnel test section



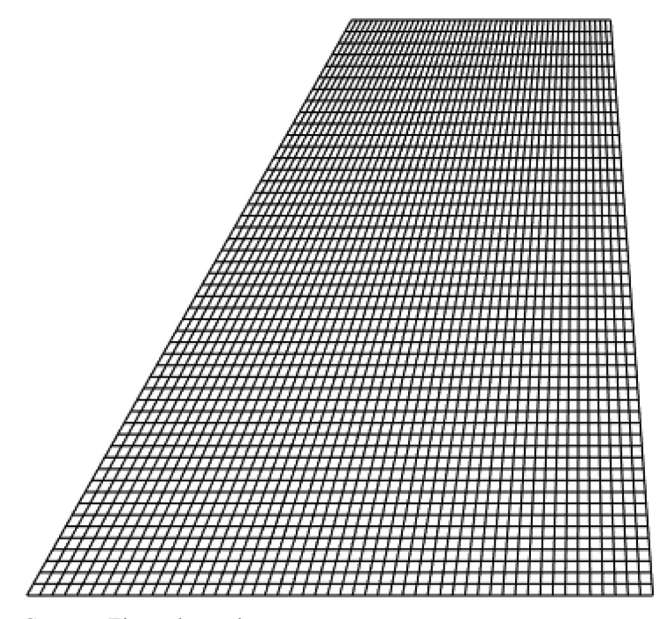




Notes: (a) The two cameras mounted outside of the test section for 3D DIC; (b) the wing model with speckle pattern for DIC; (c) splitter plate and aluminum plate mounted onto the turntable **Source:** Figure by authors

interpolation of the results between the two grids happened through finite plate splines, which is a 2D spline appropriate for aero and structural grids that are not in a single plane (MSC, 2006). An aerodynamic plane of symmetry was applied about

Figure 4 Nastran aerodynamic grid



Source: Figure by authors

the centerline at the wing root because only half-span was modeled.

Nastran computes the aerodynamic loads using the doublet lattice method (DLM). The method is based on the linear potential theory and represents the lifting surfaces as trapezoidal boxes parallel to the flow (Tewari, 2015), ignoring 3D effects and viscous flow. Despite the limitations of the DLM, this approach is less computationally expensive than computational fluid dynamics (CFD) and offers enough accuracy for the purpose of this paper, highlighted in the *Abstract* and *Introduction* sections.

2.6 Experimental validation

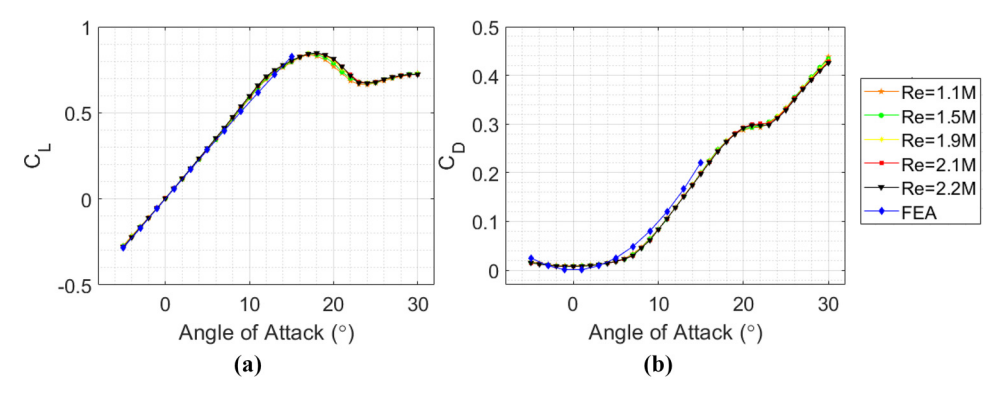
To validate the finite element model, the wing model was tested in the wind tunnel for a range of speeds from $45.7 \,\mathrm{m/s}$ to $91.4 \,\mathrm{m/s}$ and for the angles of attack from -5° to 30° . The test was run twice on different days to ensure repeatability. The aerodynamic loads were recorded, and the aerodynamic coefficients for five speeds were plotted against the angle of attack in Figure 5.

The curves of the lift coefficients versus the angle of attack are shown in Figure 5(a). There is no visible difference in the lift characteristics with respect to the free-stream speed or Reynolds number (*Re*). The lift coefficient increased linearly with the angle of attack for angles less than 12° as the attached flow is present on the wing. The stall angle of the wing is approximately 16°–18° as evidenced by a decrease of lift coefficient. Because of the leading-edge vortices (LEV) for the high-swept angle wing, the wing exhibited a mild stall beyond the stall angle. The lift coefficients flattened out when the angle was above 23°. This observation is consistent with the flow field measurement reported in Zhang *et al.* (2019).

The drag coefficients at the tested angles of attack are shown in Figure 5(b). At lower angles of attack (below 8°), the drag coefficient varies little with the angle of attack and the values are less than 0.1. However, the drag coefficient rapidly increases with

Volume 30 · Number 1 · 2024 · 73-84

Figure 5 Variation of (a) lift coefficient with angle of attack and (b) drag coefficient with angle of attack



Source: Figure by authors

the angle as the angle of the wing gets into the pre-stall region, where the lift still increases linearly with the angle. The increase in drag coefficients may be attributed to the formation of LEV at higher angles. The LEV maintains the flow attached to the wing at a pre-stall angle range; however, it also transited the boundary layer into the turbulent flow and, thus, produced higher skin friction drag. The observed results were also consistent with the study done on a subsonic 40° swept wing (Zhang et al. 2019). As shown in Figure 5, the aerodynamic characteristics of the fighter wing were independent of the *Re* as the effects of the viscous force became weaker in the *Re* range tested.

The aerodynamic coefficients as a function of the angle of attack obtained computationally were plotted against the experimental curves, demonstrating a very good agreement for the lift coefficient curve until the pre-stall region ($\alpha < 8^{\circ}$). In this range (before pre-stall), the attached flow was dominant, while the LEV was relatively weak. The experimental and computational curves for the drag coefficient were within acceptable agreement up to the stall angle. The finite element solution becomes invalid for higher angles of attack (near stall) because of its assumption of an inviscid, linear potential flow (MSC, 1987). The viscous effect becomes more critical for high angles of attack. Only one computational curve is shown in Figure 5 as the relationship between the aerodynamic coefficients and angle of attack is independent of the Re due to the inviscid potential flow used in Nastran.

A closer look at the aerodynamic parameters and coefficients is presented in Table 2 for a 10° angle of attack at which acceptable results were obtained, although it is in the transition to the pre-stall region. The experimental aerodynamic coefficients in Table 2 are the average of two runs with the per cent errors, which are very low (less than 1%), demonstrating the repeatability of the experiment. The computational and experimental results for the lift show very good agreement with less than 8% difference. However, a higher difference, yet less than 16%, is obtained for the drag coefficient. This difference derives from the inviscid model used by Nastran and the relatively small absolute values of the drag coefficient.

Another important result is the out-of-plane deflection (δ_{aero}) experimentally obtained using DIC at a sampling rate of 100 Hz for 10 s for a constant speed and 10° angle of attack. The deflection was averaged over time, and the

maximum value on the surface of the structure, which happens at the tip, is shown in Table 2. The computational and experimental results are in reasonable agreement, with a maximum difference of 13%. The difference between the two sets of results increases with the magnitude of deflection and may be related to the resolution of the DIC system that becomes less accurate for displacements larger than 20 mm. This observation results from a preliminary test done by translating a flat plate with pre-determined distances to check the set-up and calibration of the cameras before the actual test

The computational and experimental displacement contours at 45.7 m/s and 10° angle of attack are also in good agreement, as shown in Figure 6. At 91.4 m/s and 15° angle of attack, there is a 14.75% error between the maximum deformation obtained from computational and experimental. In addition, there is a slight discrepancy in the experimental and computational contours, which can be explained by the fact that the wing is close to stall, and Nastran becomes less accurate as the flow starts separating. The contours for the other speeds are similar and were omitted for the sake of succinctness. Another important observation is that the roughness produced by the specklex particles neither significantly affected the results nor compromised the validation. The aforementioned observations validate the computational aeroelastic model before the stall condition.

3. Comparison of optimized wing models

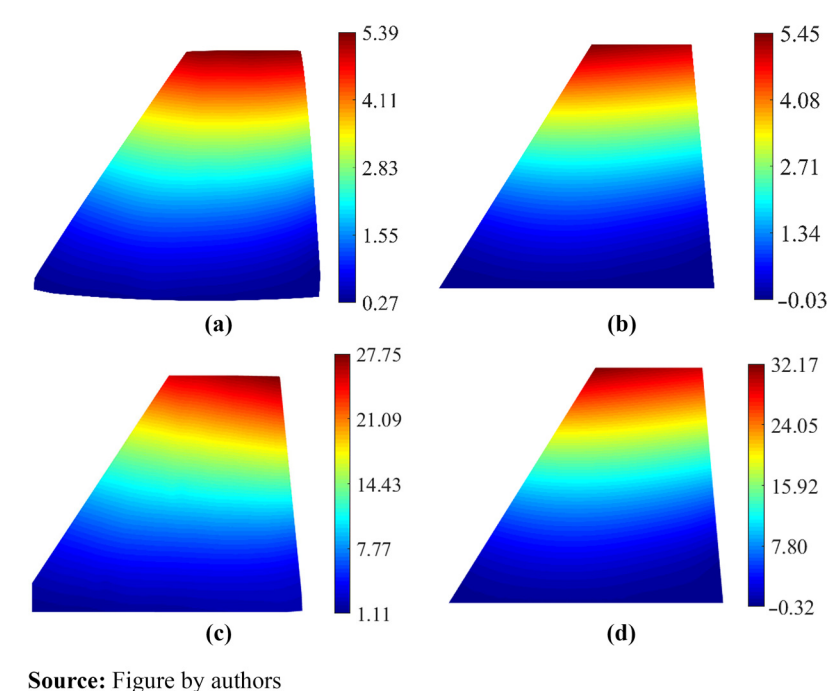
Although curvilinear spars and ribs have proved to enhance the stiffness, strength and buckling characteristics of designs (Locatelli et al., 2011), their optimization, such as spline-based optimization, can be computationally expensive. Homogenization-based topology optimization can be used to obtain the spar-rib design at a lower computational cost because the optimization is performed in a coarse mesh, and only the final optimized design is projected onto a fine mesh (2022). More complex models can be obtained by relaxing the optimization constraints. Therefore, this section uses homogenization-based topology optimization to generate four lattice wings and evaluates their performance and efficiency in comparison to the curvilinear spar-rib model. The optimization framework, developed by Wang and Tamijani (2022) and used in

Volume 30 · Number 1 · 2024 · 73–84

Table 2 Comparison of experimental and computational aerodynamic coefficients and deflection at AOA = 10°

Reynolds number, Re	Air Speed, V (m/s)	Data	Lift coefficient, C_L	Drag coefficient, C_D	Moment coefficient, C _{Mrc/4}	Deflection, δ_{aero} (mm)
1.1 M	45.7	Experimental	$0.58 \pm 0.27\%$	$0.08 \pm 0.05\%$	-0.33 ±0.67%	5.39
		FEA	0.55	0.10	-0.32	5.40
		Difference (%)	6.49	-12.89	3.36	-0.19
1.5 M	61.0	Experimental	$0.59 \pm 0.35\%$	$0.08 \pm 0.41\%$	$-0.34 \pm 0.91\%$	10.14
		FEA	0.55	0.10	-0.32	9.69
		Difference (%)	6.86	-14.59	3.98	4.54
1.9 M	76.2	Experimental	$0.59 \pm 0.60\%$	$0.08\pm0.19\%$	$-0.34 \pm 0.15\%$	16.90
		FEA	0.55	0.10	-0.32	15.28
		Difference (%)	7.68	-14.37	4.05	10.59
2.1 M	83.8	Experimental	$0.59 \pm 0.58\%$	$0.08\pm0.77\%$	$-0.34 \pm 0.11\%$	21.01
		FEA	0.56	0.10	-0.33	18.50
		Difference (%)	7.65	-14.85	4.22	12.71
2.2 M	91.4	Experimental	$0.60 \pm 0.67\%$	$0.08\pm0.53\%$	$-0.34 \pm 0.05\%$	25.15
		FEA	0.56	0.10	-0.33	22.18
		Difference (%)	7.79	-15.81	4.01	12.91
Source: Table by author	ors					

Figure 6 Out-of-plane displacement [mm] contours obtained from (a) DIC; (b) FEA at 45.7 m/s and 10° angle of attack; (c) DIC and (d) FEA at 91.4 m/s and 15° angle of attack



this section, optimizes the material and orientation of threedimensional structures by minimizing the compliance subjected to a weight constraint.

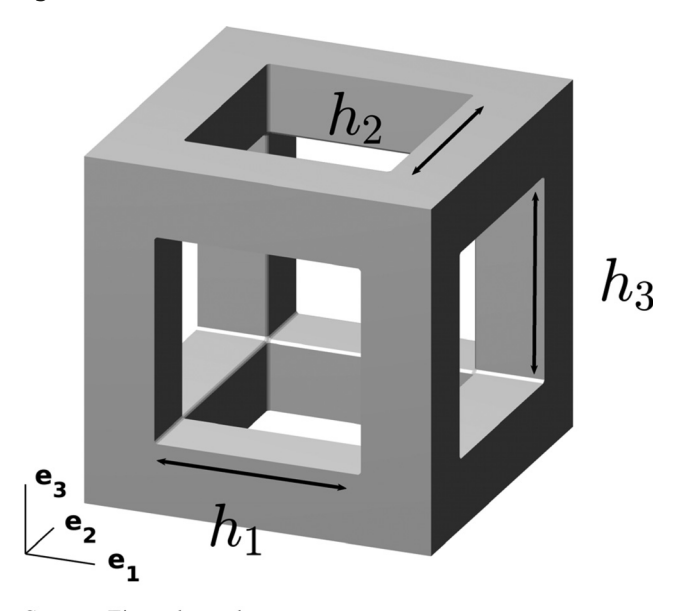
Before the optimization, the lattice type was selected and represented as a linear combination of primitive vectors (\mathbf{a}_1 , \mathbf{a}_2 and \mathbf{a}_3) in the form $m_1\mathbf{a}_1 + m_2\mathbf{a}_2 + m_3\mathbf{a}_3$, where m_1 , m_2 and m_3 are integers. For single load cases, as considered in the present study, and intermediate density, cubic lattices yielded stiffer designs and better performance because their walls conformed to the principal stress direction. For this reason,

cubic lattices were chosen. The dimensions of the hole (h_1, h_2) and h_3 in the \mathbf{e}_i vector (refer to Figure 7) were defined as parameters, and the Fourier series was used to define the unit cell. Numerical homogenization was used to determine the effective Young's Modulus for different parameters to build the response surface.

The homogenized material and cell geometry were used by an optimizer that minimizes compliance and were subjected to volume and geometric constraints based on the following mathematical representation:

Volume 30 · Number 1 · 2024 · 73–84

Figure 7 Cubic lattice



Source: Figure by authors

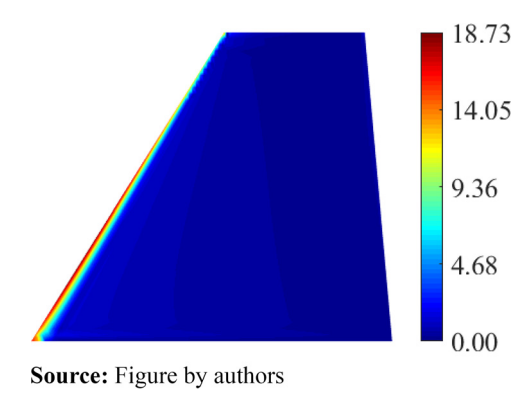
$$\min_{h_1,h_2,h_3,\theta_1,\theta_2,\theta_3} \mathcal{J}(h_1,h_2,h_3,\theta_1,\theta_2,\theta_3,\mathbf{u}) \\
= \left(\frac{\gamma_c}{\mathcal{F}^0}\right) \mathcal{F}(h_1,h_2,h_3,\theta_1,\theta_2,\theta_3,\mathbf{u}) + \left(\frac{\gamma_\theta}{P_\theta^0}\right) P_\theta(\theta_1,\theta_2,\theta_3) \\
s.t.: \mathbf{K}(h_1,h_2,h_3,\theta_1,\theta_2,\theta_3) \mathbf{u} = \mathbf{f}, \\
: \frac{1}{V} \int_{\Omega} \rho(h_1,h_2,h_3) d \Omega - V_f^{\max} \leq 0, \\
: 0 \leq h_1,h_2,h_3 \leq 1, \\
: -4\pi \leq \theta_1,\theta_2,\theta_3 \leq 4\pi,$$
(1)

where \mathcal{F}^0 , γ_c and γ_θ are the initial compliance and the weights assigned to the compliance, respectively. θ_1 , θ_2 and θ_3 are the Euler angles used to represent the cell orientation. **f**, **u** and **K** denote the load vector, the displacement vector and the global stiffness matrix, respectively. V, V_f^{max} and ρ represent the volume of the design domain, the allowed volume fraction and the density function, respectively. A penalty function, P_{θ} , is introduced to penalize abrupt changes in adjacent elements, and its initial value is P_{θ}^0 .

This optimization problem was solved using the method of moving asymptotes, and the code was parallelized in FreeFem++ using MPI. After optimization, the coherent orientation in the design domain was determined by checking the direction of each element, as described by Wang and Tamijani (2022). The design is projected onto a fine mesh, and the projection requires post-processing to smooth the surface, remove floating members and impose a minimum feature size.

The volume fraction of the internal structure was set as 10% to match the weight of the spar-rib structure. The distributed load resulting from the divergence analysis of the spar-rib wing model at an airspeed of 45.7 m/s and 10° angle of attack was imported from MSC. Nastran into the optimizer code. The aerodynamic load (Figure 8) shown as the coefficient of pressure was more predominant on the leading edge while the wing root was clamped. The projected inner structures are shown in Figure 9, from which it is clearly visible that the optimizer places the

Figure 8 Pressure coefficient (C_p) distribution at 45.7 m/s and 10° angle of attack



material predominantly at the leading edge where the load is larger.

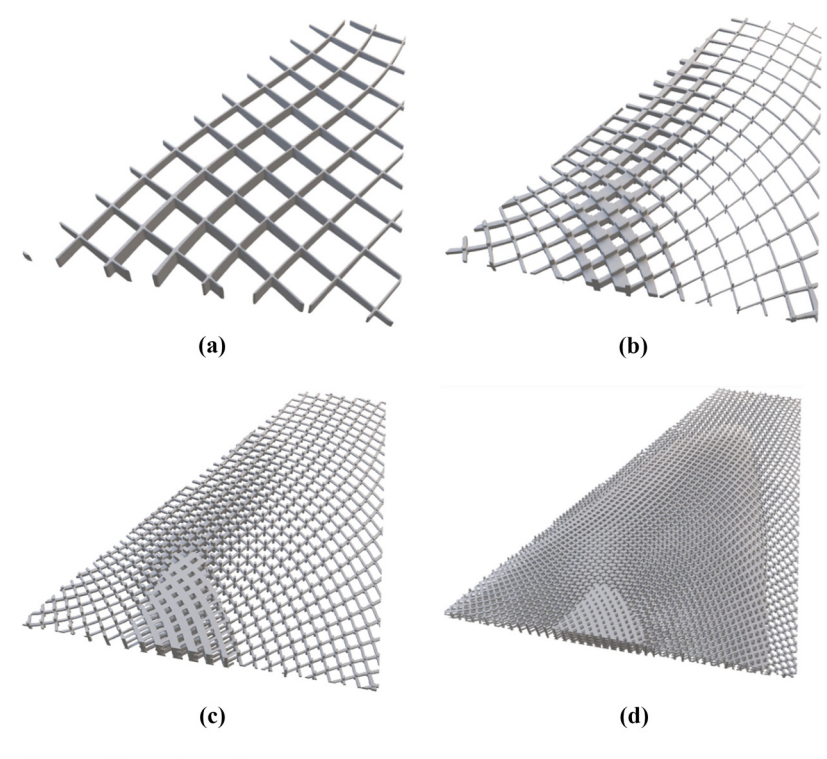
For the first lattice model [Figure 9(a)], a simpler design with solid walls along \mathbf{e}_3 , similar to the spar-rib design, was obtained by fixing the size of the lattice hole along \mathbf{e}_3 to a constant value of $h_3 = 0.00$ and the cell size to $\Lambda = 40$. More detailed models were created by allowing h_3 to vary for the other three lattice wing models [Figure 9(b)–(d)], for which three cell sizes were considered ($\Lambda = 30,15$ and 7.50). The projection parameter Λ significantly affects the final projected design and performance, as discussed later in this section. The projection parameter Λ has no impact in the \mathbf{e}_3 direction for the first lattice wing model as $h_3 = 0.00$. However, it affects the other three wing designs, Figure 9(b)–(d), in all three directions.

The optimizer produces an STL of the optimized internal structure, which needs to be combined with the skin (Figure 10). Due to the geometric complexity of the models, converting the model into a solid CAD model and meshing it can be challenging, requiring several steps of cleaning and simplification. Therefore, Meshlab was initially used to simplify the internal structure model and remove duplicate surfaces. Then, 3D builder or Ansys SpaceClaim was used to check and fix errors, such as fixing surface orientation, filling holes and solving nonmanifold errors. The clean model was re-meshed, solving self-intersecting errors and reducing the number of triangles to less than 3 million elements, which was sufficient for the inner structures in this study. SpaceClaim was once again used to address any remaining self-intersecting and nonmanifold errors. The step file of the skin was imported into Gmsh, meshed and saved as an STL, which was combined with the inner structure in SpaceClaim. Meshmixer was used to re-mesh and reduce the size of the combined model before being converted into a solid model in SpaceClaim. The root of the models was closed with a thin plate to reduce the impact of the boundary condition because some of the members of the internal structure of the wing in Figure 9(b)-(d) were not connected to the root. Finally, the CAD model was meshed in ANSYS using Tetra 10 elements, and the mesh was analyzed in MSC. Nastran.

The mesh convergence is shown in Table 3. Based on the convergence of the aeroelastic deformation (δ_{aero}), the mesh considered for each wing model had between 1.3 M and 1.7 M elements. The 1%–5% increase in the displacement by adding approximately 1 M elements would come at the cost of at least

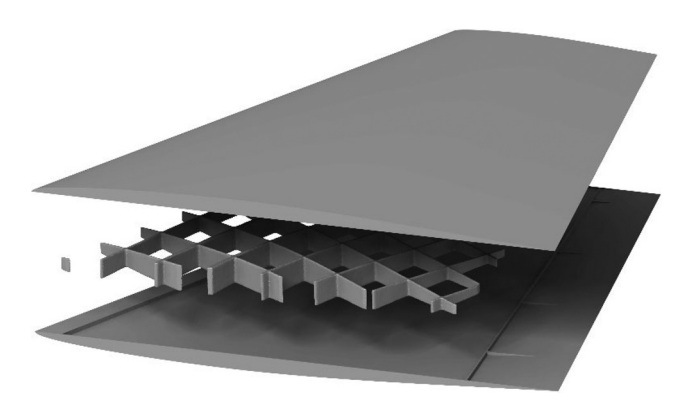
Volume 30 · Number 1 · 2024 · 73–84

Figure 9 (a) Projected lattice wing internal structure for fixed $h_3 = 0.00$ and $\Lambda = 40$; (b) projected lattice wing internal structure for variable h_3 and $\Lambda = 30$; (c) projected lattice wing internal structure for variable h_3 and $\Lambda = 7.50$



Source: Figure by authors

Figure 10 Representation of lattice internal structure involved by wing skin



Source: Figure by authors

double the computational time. The computational time naturally increases for the lattice wing models due to their elaborated geometry.

The above-mentioned iterative process could be time-consuming, and it highly depends on the complexity of the STL model. The complexity of the model with optimized topology and orientation will increase if the projected parameter Λ is decreased.

To evaluate the performance of the aforementioned wings, their computational displacements were compared for two load conditions:

- a distributed static load of 500 N on the top skin; and
- 2 an airflow of 45.7 m/s at a 10° angle of attack, which produces around 180 N of lift.

The models were constrained similarly to the spar-rib wing model previously described in section 2.5. The five wings have the same aerodynamic coefficients, $C_L = 0.097$, $C_D = 0.547$ and $C_M =$ -0.323, because the aeroelastic analysis is performed using DLM, and in which the wing model is represented as a trapezoidal surface without any consideration of the internal structure. Table 4 shows the displacements and stiffness resulting from the two load cases for the five wing models. The stiffnesses from the static analysis (K_{eff}^s) and from the static aeroelastic (divergence) analysis $(K_{\it eff}^d)$ were defined as the sum of the forces at each node (F = 500 N for the static load case and F = 180 N for the divergence analysis) divided by the maximum displacement ($\delta_{max} = \delta_{static}$ for static load case and $\delta_{max} = \delta_{aero}$ for the aeroelastic analysis) and divided by the volume fraction $(K_{eff} = \frac{F}{V_f \delta_{max}})$. For the static load case, the results clearly show that the lattice wing model with constant $h_3 = 0.00$ is stiffer than the curvilinear spar-rib model for a 2.60% increase in volume.

Relaxing the design parameters like in the lattice wings with $\Lambda=30$, 15 and 7.50, allows a more efficient material distribution over a larger region and theoretically higher stiffness. However, the stiffness is highly affected by Λ as well. As the parameter Λ approaches 0, the projected result converges to the homogenized result. The large projection parameter of $\Lambda=30$ makes the projected results differ from the homogenized results. Because it is all solid, the first lattice wing (for $h_3=0.00$) has infinite cells in the e_3

Volume 30 · Number 1 · 2024 · 73–84

Table 3 Mesh convergence for the five models considered in this paper

Model	No. of elements	δ_{aero} (mm)	Computational time (min)
Spar-ribs wing	0.8 M	5.27	80
	1.3 M	5.40	155
	2.5 M	5.46	330
Lattice wing $h_3 = 0.00$	1.3 M	5.15	180
	1.7 M	5.22	250
	2.5 M	5.43	660
Lattice wing $\Lambda = 30$	0.7 M	6.07	70
-	1.5 M	6.09	190
	2.5 M	6.44	660
Lattice wing $\Lambda = 15$	1.4 M	5.46	190
-	2.3 M	5.63	660
	2.5 M	5.70	800
Lattice wing $\Lambda = 7.50$	1.9 M	4.73	225
-	2.2 M	4.87	670
	2.5 M	4.92	900
Source: Table by authors			

Table 4 Comparison of displacements between curvilinear spar-rib model and lattice wings

	Volume fraction, V_f (%)	Static displacement, $\delta_{\it static}$ (mm)	Static stiffness, $\mathbf{K}_{\mathrm{eff}}^{\mathrm{s}}(\text{N/mm})$	Aeroelastic displacement, δ_{aero} (mm)	Aeroelastic stiffness, $K_{\rm eff}^{\rm d}$ (N/mm)
Spar-ribs wing	38	20.80	63.26	5.40	87.72
Lattice wing $h_3 = 0.00$	39	18.60	68.93	5.15	89.62
Lattice wing $\Lambda = 30$	42	22.80	52.21	6.09	70.37
Lattice wing $\Lambda = 15$	43	19.60	59.33	5.46	76.67
<i>Lattice Wing</i> $\Lambda = 7.50$	43	13.60	85.50	4.87	85.96
Source: Table by authors					

direction. However, this is not the case for the second lattice wing ($\Lambda=30$). The maximum thickness of the root airfoil is 32 mm (Table 1). Therefore, for the projection parameter $\Lambda=30$, most of the regions in the third wing have less than one unit cell occurring in the e_3 direction. The minimum number of unit cells needed in each direction to make the projected design achieve a similar performance as the homogenized design is 10. Moreover, the static and aerodynamic loads are mainly applied in the e_3 direction. Therefore, the number of unit cells in the e_3 direction significantly impacts the performance of the projected design, as demonstrated in Table 4. As Λ decreases, the stiffness increases. Therefore, the fourth lattice model for which $\Lambda=7.50$ shows a significant improvement in stiffness.

The displacement contours, shown in Figure 11, for the airspeed of 45.7 m/s at 10° of the angle of attack are similar for all four lattice wings and compared to the spar-rib model (Figure 6). Under this load, the models are under bending, for which the tip of the leading edge experiences the maximum displacement.

4. Conclusion

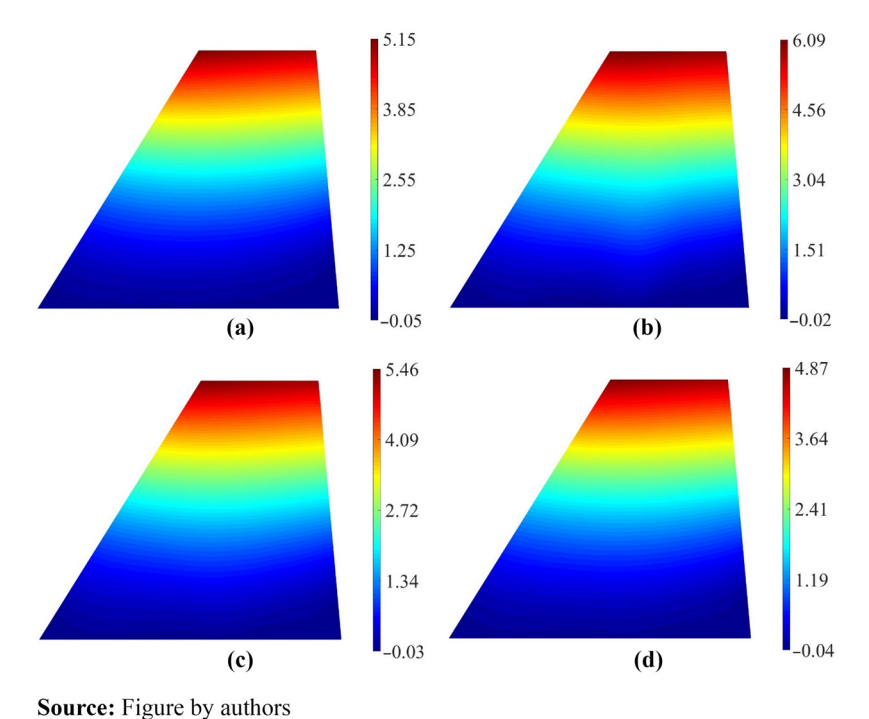
A flexible fighter wing model with curvilinear spars and ribs has been additively manufactured to assess the feasibility of 3D-printed wind tunnel models and the practicability of

the optimized design. A finite element analysis framework has been created to predict the aeroelastic response of the model in the wind tunnel. To validate the computational model, the fighter wing was tested in the wind tunnel for a range of speeds from 45.7 m/s to 91.4 m/s and for 36 angles of attack from -5° to 30° . The yaw, pitch and roll angles were kept constant at zero. The test was run twice on different days to ensure repeatability. The aerodynamic loads and moments were recorded, and the aerodynamic coefficients for five speeds were plotted against the angle of attack and compared with the curves from computational data. Another important result was the out-of-plane deflection (δ_{aero}) experimentally obtained using DIC, which was also used to validate the computational model. The computational and experimental results were in good agreement, within a 17% difference.

Curvilinear spars and ribs are known to improve the stiffness of models when compared to traditional spars and ribs, but their optimization can be computationally expensive. Therefore, homogenization-based topology optimization, which is more computationally efficient, was used to generate four-wing models. By comparing the stiffness of the five wings, it was clear that the performance of the models is tightly related to the lattice parameters h_1 , h_2 and h_3 and the cell size Λ . The manipulation of those can lead to designs with a higher stiffness than the curvilinear spar-rib wing.

Volume 30 · Number 1 · 2024 · 73-84

Figure 11 Out of plane displacement (mm) contour for (a) lattice wing with $h_3 = 0.00$; (b) lattice wing with $\Lambda = 30$; (c) lattice wing with $\Lambda = 15$; and (d) lattice wing with $\Lambda = 7.50$



The present work demonstrated the practicability and accuracy of AM wind tunnel models and the feasibility of homogenization-based topology optimization to generate designs with enhanced stiffness.

References

Abbott, I.H. and Von Doenhoff, A.E. (2012), *Theory of Wing Sections: including a Summary of Airfoil Data*, 1st ed., Dover, New York.

Aghanajafi, C. and Daneshmand, S. (2010), "Integration of three-dimensional printing technology for wind-tunnel model fabrication", *Journal of Aircraft*, Vol. 47 No. 6, pp. 2130-2135.

Barlow, J.B., Rae, W.H. and Pope, A. (1999), Low-Speed Wind Tunnel Testing, 3rd ed., John Wiley & sons, New York, NY.

Chung, H.S., Kim, S.P. and Choi, Y. (2020), "Using additive manufactured parametric models for wind tunnel test-based aerodynamic shape optimization", *Rapid Prototyping Journal*, Vol. 27 No. 1.

Del Carre, A., Muñoz-Simón, A., Goizueta, N. and Palacios, R. (2019), "SHARPY: a dynamic aeroelastic simulation toolbox for very flexible aircraft and wind turbines", Journal of Open Source Software, Vol. 4 No. 44, p. 1885.

Diebold, J.M., Woodard, B., Monastero, M. and Bragg, M. (2015), "Experimental study of splitter plates for use with Semispan wing models", 53rd AIAA aerospace sciences meeting, 1227.

Fernandes, R.R. and Tamijani, A.Y. (2017), "Flutter analysis of laminated curvilinear-stiffened plates", *AIAA Journal*, Vol. 55 No. 3, pp. 998-1011.

Fernandes, R.R., Tamijani, A.Y. and Al-Haik, M. (2021), "Mechanical characterization of additively manufactured fiber-reinforced composites", *Aerospace Science and Technology*, Vol. 113, p. 106653.

Goh, G., Agarwala, S., Goh, G., Dikshit, V., Sing, S.L. and Yeong, W.Y. (2017), "Additive manufacturing in unmanned aerial vehicles (UAVs): challenges and potential", *Aerospace Science and Technology*, Vol. 63, pp. 140-151.

Junk, S., Schröder, W. and Schrock, S. (2017), "Design of additively manufactured wind tunnel models for use with UAVs", *Procedia CIRP*, Vol. 60, pp. 241-246.

Kroll, E., Artzi, D. and Ralbag, G. (2010), "Structural design guidelines for wind tunnel models made by rapid prototyping", 27th International Congress of the Aeronautal Sciences, Nice, France, 2010-3.2.

Locatelli, D., Mulani, S.B. and Kapania, R.K. (2011), "Wingbox weight optimization using curvilinear spars and ribs (SpaRibs)", *Journal of Aircraft*, Vol. 48 No. 5, pp. 1671-1684.

MSC (1987), "Aeroelastic analysis user's guide", available at: https://simcompanion.mscsoftware.com/infocenter/index? page=content&id=DOC9182

MSC (2006), "MSC FlightLoads and dynamics user's guide [online]".

Pankonien, A.M., Reich, G.W., Lindsley, N. and Smyers, B. (2017), "3D-printed wind tunnel flutter model", 58th AIAA/ ASCE/AHS/ASC Structures, Structural Dynamics, and Materials Conference, p. 411.

Raza, A., Farhan, S., Nasir, S. and Salamat, S. (2021), "Applicability of 3D printed fighter aircraft model for subsonic wind tunnel", 2021 International Bhurban Conference on Applied Sciences and Technologies (IBCAST), Islamabad, Pakistan. IEEE, 730-735.

Volume 30 · Number 1 · 2024 · 73-84

- Rêgo, I. D., Marcos, T.V., Galvão, V.A., Vilela, R.G., Minucci, M.A., Martos, J.F. and Oliveira, A.C. (2018), "Preliminary studies on hypersonic flows over 3D printed models", 22nd AIAA International Space Planes and Hypersonics Systems and Technologies Conference, p. 5321.
- Su, W. and Cesnik, C.E. (2011), "Strain-based geometrically nonlinear beam formulation for modeling very flexible aircraft", *International Journal of Solids and Structures*, Vol. 48 No. 16-17, pp. 2349-2360.
- Tewari, A. (2015), Aeroservoelasticity, 1st ed., Springer, Cham. Thompson, B. and Whitelaw, J. (1988), "Flow-around airfoils with blunt, round, and sharp trailing edges", Journal of Aircraft, Vol. 25 No. 4, pp. 334-342.
- Tsushima, N., Tamayama, M., Arizono, H. and Makihara, K. (2021), "Geometrically nonlinear aeroelastic characteristics of highly flexible wing fabricated by additive manufacturing", Aerospace Science and Technology, Vol. 117, p. 106923.
- Wang, Z. and Tamijani, A.Y. (2022), "Computational synthesis of large-scale three-dimensional heterogeneous lattice structures", Aerospace Science and Technology, Vol. 120, p. 107258.
- Zhang, S., Jaworski, A.J., McParlin, S. and Turner, J.T. (2019), "Experimental investigation of the flow structures over a 40 swept wing", *The Aeronautical Journal*, Vol. 123 No. 1259, pp. 39-55.
- Zhu, W. (2019), "Models for wind tunnel tests based on additive manufacturing technology", *Progress in Aerospace Sciences*, Vol. 110, p. 100541.
- Zhu, W., Miao, K. and Li, D. (2019a), "Static aeroelastic models with integrated stiffness-contributing shell structures built by additive manufacturing", *Engineering Structures*, Vol. 187, pp. 352-361.
- Zhu, W., Zhang, X. and Li, D. (2019b), "Flexible all-plastic aircraft models built by additive manufacturing for transonic wind tunnel tests", Aerospace Science and Technology, Vol. 84, pp. 237-244.

Further reading

- Banks, J., Giovannetti, L.M., Soubeyran, X., Wright, A., Turnock, S. and Boyd, S. (2015), "Assessment of digital image correlation as a method of obtaining deformations of a structure under fluid load", *Journal of Fluids and Structures*, Vol. 58, pp. 173-187.
- Katzenmeier, L., Vidy, C., Kolb, A. and Breitsamter, C. (2021), "Aeroelastic wind tunnel model for tail buffeting

- analysis using rapid prototyping technologies", CEAS Aeronautical Journal, Vol. 12 No. 3, pp. 1-19.
- Kuester, M., Intaratep, N. and Borgoltz, A. (2018), "Laser displacement sensors for wind tunnel model position measurements", *Sensors*, Vol. 18 No. 12, p. 4085.
- Livne, E. (2018), "Aircraft active flutter suppression: state of the art and technology maturation needs", *Journal of Aircraft*, Vol. 55 No. 1, pp. 410-452.
- Stanford, B. (1688), "Topology optimization of low-speed aeroelastic wind tunnel models", AIAA Scitech 2021 Forum.

About the authors

Rossana Fernandes received her PhD degree from Embry-Riddle Aeronautical University. Her research interests are additively manufacturing materials and optimized composite structures.

Benyang Hu received his Master of Science in Aerospace Engineering from Embry-Riddle Aeronautical University. His research focus is on stress analysis, digital processing, topology optimization and design.

Zhichao Wang received his PhD degree from Embry-Riddle Aeronautical University. His research focus is on 3D large-scale topology and morphology topology design of compliance and stress problems.

Zheng Zhang is an active researcher in experimental aerodynamics, fluid-structure interaction and developing relevant instrumentation for low-speed wind tunnel testing. He obtained his PhD degree in Aerospace Engineering and Mechanics from the University of Alabama in 2014. Currently, he is a senior research scientist at the Department of Aerospace Engineering at Embry-Riddle Aeronautical University, working primarily in ERAU's 6-by-4 ft low-speed wind tunnel.

Ali Y. Tamijani is a Professor in the Department of Aerospace Engineering at Embry-Riddle Aeronautical University. His research has been focused on innovative lightweight and efficient structural designs using novel analysis techniques, robust optimization algorithms, coupled with advanced manufacturing processes. Ali Y. Tamijani is the corresponding author and can be contacted at: tamijana@erau.edu